King's Research Portal

Micro-networks for robust MR-guided low count PET imaging

Casper O. da Costa-Luis, *Student Member, IEEE,* and Andrew J. Reader

Abstract—Noise suppression is particularly important in low count PET imaging. Post smoothing (PS) and regularisation methods which aim to reduce noise also tend to reduce resolution and introduce bias. Alternatively, anatomical information from another modality such as magnetic resonance (MR) imaging can be used to improve image quality. Convolutional neural networks (CNNs) are particularly well suited to such joint image processing, but usually require large amounts of training data and have mostly been applied outside the field of medical imaging or focus on classification and segmentation, leaving PET image quality improvement relatively understudied. This work proposes the use of a relatively low-complexity CNN (micro-net) as a post-reconstruction MR-guided image processing step to reduce noise and reconstruction artefacts while also improving resolution in low count PET scans. The CNN is designed to be fully 3D, robust to very limited amounts of training data, and to accept multiple inputs (including competitive denoising methods). Application of the proposed CNN on simulated low ($30\,\mathrm{M}$) count data (trained to produce standard ($300\,\mathrm{M}$) count reconstructions) results in a $36\,\%$ lower normalised root mean squared error (NRMSE, calculated over 10 realisations against the ground truth) compared to maximum likelihood expectation maximisation (MLEM) used in clinical practice. In contrast, a decrease of only $25\,\%$ in NRMSE is obtained when an optimised (using knowledge of the ground truth) PS is performed. A $26\,\%$ NRMSE decrease is obtained with both RM and optimised PS. Similar improvement is also observed for low count real patient datasets. Overfitting to training data is demonstrated to occur as the network size is increased. In an extreme case, a U-net (which produces better predictions for training data) is shown to completely fail on test data due to overfitting to this case of very limited training data. Meanwhile, the resultant images from the proposed CNN (which has low training data requirements) have lower noise, reduced ringing and partial volume effects, as well as sharper edges and improved resolution compared to conventional MLEM.

Index Terms—Machine Learning, Deep Learning, Convolutional Neural Network, Resolution Modelling, Resolution Recovery, Image Processing, MLEM, Image Reconstruction, Guided Reconstruction, PET, MR.

I. Introduction

POSITRON emission tomography (PET) image reconstruction is an ill-posed inverse problem, for which maximum likelihood expectation maximisation (MLEM) is a commonly used iterative reconstruction method. Advantages of MLEM include the ability to incorporate a model of the entire acquisition process including, for example, attenuation and scatter.

Lowering the injected radioactive dose and/or overall scan time results in fewer acquired counts. Noise suppression becomes particularly important in the case of low count scans. As the sinogram data is inherently Poisson in distribution [1], both signal and variance are related to the total number of counts. Signal to noise ratio (SNR) thus is related to the root of the total number of counts [2]. Low count scans therefore result in images with high levels of noise.

Marked improvement in image detail (resolution and contrast recovery) and visual noise suppression can be achieved through use of resolution modelling (RM), apparently leading to better lesion detectability under certain conditions [3]–[6]. However, RM can also introduce ringing artefacts. The resultant visual impact on reconstructed images is extra edges parallel to those already in the image. These artefacts can greatly exaggerate maximum standardised uptake values ($\mathrm{SUV_{max}}$) which can lead to overestimation of tumour aggressiveness [7], [8]. There is therefore debate as to whether RM should even be used at all [5]. Under-modelling of resolution, post-smoothing (PS) [9], and regularisation methods (such as total variation de-noising [10]) can compensate for reconstruction artefacts. However, these methods tend to degrade resolution or edge accuracy.

Alternatively, simultaneously acquired CT (computed tomography) or MR data – which typically have lower noise – can be used in techniques such as non-local means (NLM) to reduce noise in PET reconstructions [11]. Kernelised methods may even be incorporated into the MLEM reconstruction process [12].

This work proposes an alternative post-processing step informed by deep learning (DL) – specifically, deep convolutional neural networks (CNNs). CNNs are multi-layer frameworks capable of learning high-level image features from pixel data. This builds on the concept of sparse

representation of features used in dictionary learning approaches [13], [14]. CNNs are particularly suited to image processing tasks and have garnered much excitement in the computer science community. Meanwhile CNNs applied to medical imaging have primarily focused on classification and segmentation [15], [16], and have left PET, in particular, relatively understudied [17]. Uptake of CNNs for medical imaging quality improvement has been comparatively recent and modest [18], [19], and typically applied to 2D slices and/or patches [20]–[22]. Some proposals include combining DL with an unfiltered backprojection as a faster, comparable alternative to iterative MLEM reconstruction [23], while others suggest 2D patch-based methods to reduce noise in low-dose PET-CT [24] and PET-MR reconstructions [25]. Recently, CNNs have also been incorporated into iterative reconstruction [26], [27]. CNN architectures are particularly well suited to using the increased resolution available in jointly acquired MR or CT data to reduce the noise in PET reconstructions. However, such networks typically require large amounts of training data and suffer from computational memory constraints.

For low dose PET-MR, small (5^3) 3D patches have been used in sparse dictionary-based approaches [28], [29]. For fully 3D low dose PET-MR, non-CNN approaches such as regression forests have also been applied in prior work [30].

In contrast, this work focuses on improving image quality through 3D CNNs which are flexibly designed to use MR guidance for reduced dose PET imaging, as well as remove reconstruction artefacts. Alternative methods may be used as additional network input channels, which should ensure superior performance. The primary aim is to reduce noise, while resolution improvement is secondary. Due to the design and resultant small size of the networks used here, we propose the term micro-network, or μ-net. These μ-nets have a comparatively small parameter space and thus are robust against overfitting on extremely limited training data sets, in stark contrast to the U-nets found in the current literature [31], [32].

II. METHODS

The proposal is to use a neural network to improve the quality of low count reconstructions. Three cases are considered. Initially, a network is trained to map low count simulations to the ground truth. Secondly, the same network architecture is retrained to map to standard count reconstructions instead. Finally, this latter case is repeated with real patient data. The following section starts with a description of the simulated data.

A. MLEM

1) Simulations: MR-based *BrainWeb* segmentations of 20 subjects [33] were modified to have [18F]FDG PET-like intensities (contrast ratio 4:1 for grey to white matter, 0.5:1 for dura, and ranging from 6:1 to 8:1 for spherical lesions of 5 to 15 mm in diameter and varying sharpness which were introduced into the phantom). The positions and sizes of

these lesions were randomised [34]. Attenuation maps were generated with factors of 0.13 and 0.0975 for bone and tissue, respectively, and added to scanner manufacturer-provided hardware maps. Some randomised structure was also introduced for the PET and MR segmentations according to Equation (1) to produce a realistic non piece-wise constant phantom $\boldsymbol{\tau}$, given by:

$$\boldsymbol{\tau} = \boldsymbol{\phi} \circ (\mathbf{1} + \gamma[2G_\sigma(\boldsymbol{\rho}) - \mathbf{1}]) \tag{1}$$

where $\boldsymbol{\tau}$ is used as a realistic ground truth phantom for the simulations,
   $\boldsymbol{\phi}$ is a *BrainWeb*-based segmented phantom,
   γ is an intensity parameter chosen to be 1.5 for PET and 1 for MR segmentations,
   G_σ represents Gaussian smoothing of $\sigma = 1$ pixel,
   $\boldsymbol{\rho}$ is of the same size as $\boldsymbol{\phi}$ with random uniform distributed elements $\in [0, 1)$, and
   $\circ$ is the Hadamard (element-wise) product.

For each phantom, resolution degradation effects were simulated in image space by smoothing with a Gaussian with 4.5 mm FWHM (full width at half maximum). A forward projector from *NiftyPET* [35] was then used to simulate 837 span 11 sinograms $\boldsymbol{m}$. Simulations correspond to the Siemens Biograph mMR scanner ($2.09 \times 2.09 \times 2.03\,\mathrm{mm}^3$ voxel size and image dimensions $344 \times 344 \times 127$), accounting for photon attenuation and normalisation (including geometry, crystal efficiencies, and dead time effects as described in [35]).

Count levels were varied from 3 M up to a maximum of 300 M (including 26 % randoms and 28 % scatter). The maximum count level was chosen to be comparable to that of real data (for a scan of 20 min with 370 MBq injected activity). Ten Poisson noise realisations were generated for each noise level, followed by MLEM reconstructions. Each iteration k of the reconstructed image $\boldsymbol{\theta}$ is given by:

$$\boldsymbol{\theta}^{(k+1)} = \frac{\boldsymbol{\theta}^{(k)}}{\boldsymbol{H}^T \boldsymbol{X}^T \mathbf{1}} \circ \boldsymbol{H}^T \boldsymbol{X}^T \frac{\boldsymbol{m}}{\boldsymbol{X}\boldsymbol{H}\boldsymbol{\theta}^{(k)} + \boldsymbol{\varrho}}, \tag{2}$$

where $\boldsymbol{\theta}^{(k)}$ is the reconstructed image at the kth iteration,
   $\boldsymbol{H}$ can be used to include an RM kernel,
   $\boldsymbol{X}$ is the rest of the system matrix (forward projection including attenuation and normalisation),
   $\boldsymbol{m}$ is the sinogram data,
   $\boldsymbol{\varrho}$ represent randoms and scatter, and
   division is Hadamard (performed element-wise).

For all data sets, 300 MLEM iterations were performed with RM, and 100 iterations without RM ($\boldsymbol{H} = \boldsymbol{I}$ in Equation (2)). More iterations are required for RM due to its lower rate of convergence. RM reconstructions use a Gaussian point spread function (PSF) of 4.5mm FWHM in image space. Corresponding MR data was obtained

by adding randomised structure (Equation (1)) to the T1 *BrainWeb* phantoms and downsampling to the same resolution and dimensions as the PET reconstructions. The randomised structure ensures that a simple mapping from T1 to ground truth PET is not possible.

As a reference method, reconstruction results are post-smoothed with a Gaussian kernel. It should be noted that smoothing using a kernel at least as large as the PSF has long been proposed as a way of obviating ringing artefacts [9], [36].

A further reference is provided by modifying the non-local means (NLM) algorithm [37] to perform MR-guided Gaussian-weighted filtering using the T1-weighted recon-struction $\boldsymbol{\theta}^{(\mathrm{T1})}$. The NLM output is defined to be:

$$\mathrm{NLM}\left(\theta_j^{(k)}\right) = \frac{\sum_{i \in N_j} w_{i,j} \theta_j^{(k)}}{\sum_{i \in N_j} w_{i,j}}, \tag{3}$$

$$w_{i,j} = \exp\left\{-\frac{1}{2}\left(\frac{\theta_i^{(\mathrm{T1})} - \theta_j^{(\mathrm{T1})}}{\Omega}\right)^2\right\}, \tag{4}$$

where $\theta_j^{(k)}$ is the jth voxel of a MLEM PET reconstruction from Equation (2),
$w_{i,j}$ is a T1-derived weighting factor,
N_j is the $5 \times 5 \times 5$ neighbourhood around j,
$\theta_i^{(\mathrm{T1})}$ is the ith voxel of the T1-weighted MR reconstruction, and
Ω is an optimisation parameter.

Ten noise realisations and reconstructions are performed for all phantoms to enable calculation of standard deviation values σ across realisations. Bias b and normalised root mean squared error (NRMSE) ϵ are also calculated. These metrics are all normalised as in [38]. Normalisation is done in a manner which avoids element-wise division (thereby avoiding exaggeration from low intensity values) and to be consistent with $\epsilon^2 = \sigma^2 + b^2$:

$$b = \frac{100\%}{\sqrt{\sum_j T_j^2}} \sqrt{\sum_j \left(T_j - \mathop{\mathrm{E}}_r\{\theta_{r,j}\}\right)^2}, \tag{5}$$

$$\sigma = \frac{100\%}{\sqrt{\sum_j T_j^2}} \sqrt{\sum_j \mathop{\mathrm{Var}}_r\{\theta_{r,j}\}}, \text{ and} \tag{6}$$

$$\epsilon = \frac{100\%}{\sqrt{\sum_j T_j^2}} \sqrt{\sum_j \mathop{\mathrm{E}}_r\left\{(T_j - \theta_{r,j})^2\right\}}, \tag{7}$$

where $\theta_{r,j}$ is the jth voxel of the rth reconstruction (from the rth noise realisation),
$\mathop{\mathrm{E}}_r\{\cdot\}$ is the mean operator across r,
$\mathop{\mathrm{Var}}_r\{\cdot\}$ is the variance operator across r,
T_j is the jth target voxel,
b is normalised bias,
σ is normalised standard deviation, and

ϵ is normalised root mean squared error (NRMSE).

2) Real data: Real data $\boldsymbol{m}$ was also obtained from 10 [^{18}F]FDG PET head scans using the same scanner. Count levels varied from $400\,\mathrm{M}$ to $500\,\mathrm{M}$. Using *NiftyPET*, listmode data is randomly sampled with replacement (bootstrap method from [39]) at $300\,\mathrm{M}$ (standard), $30\,\mathrm{M}$ (low), and $3\,\mathrm{M}$ (very low) counts for each patient to ensure consistent count levels and similar distributions. Randoms were estimated through variance reduction of delayed coincidences [40], while scatters were updated (using a single-scatter model) at each MLEM iteration. On average, it was estimated that $28\,\%$ of the counts were scatter and $26\,\%$ were randoms. Each count level is sampled 10 times for estimation of standard deviation for comparison purposes.

Reconstructions were performed using the same method as with simulations (MLEM as per Equation (2)). The original raw listmode data (without bootstrap sampling) was also reconstructed for each patient in lieu of a known ground truth reference.

Corresponding MPRAGE T1 reconstructions were scaled and registered to the full count PET reconstructions using *dipy* [41] before performing NLM filtering on the PET reconstructions (Equation (3)).

B. Deep Convolutional Neural Networks

In this section, the low count PET reconstructions are combined with the corresponding MR reconstruction to form the network training input $\boldsymbol{\alpha}^{(1)}$ in Equation (8) below. The network parameters are then optimised to minimise the difference between the current output (for layer $j = 4$, this is $\boldsymbol{\alpha}^{(4)}$) and the desired target $\boldsymbol{T}$. This target may be either the ground truth $\boldsymbol{\tau}$ (if available) or standard (300 M) count reconstruction $\boldsymbol{\theta}_{\mathrm{std}}^{(100)}$. For comparison, the Gaussian post-smoothing FWHM and the NLM parameter Ω are also both optimised on the same data.

1) Layers: Each layer j of the network transforms its input vector $\boldsymbol{\alpha}^{(j)}$ as shown in Equation (8).

$$\boldsymbol{\alpha}_{k,r}^{(j+1)} = A_j\left(\beta_k^{(j)}\mathbf{1} + \sum_{i=1}^{n_{j-1}} \boldsymbol{\kappa}_{i,k}^{(j)}\boldsymbol{\alpha}_{i,r}^{(j)}\right) \quad \forall k \in [1, n_j], \tag{8}$$

where $\boldsymbol{\alpha}_{i,r}^{(j)}$ is the ith channel of the rth low count noise realisation input for layer j, such that $\boldsymbol{\alpha}^{(1)}$ represents the network's inital input volumes,
$\boldsymbol{\kappa}_{i,k}^{(j)}$ is a matrix applying the kth kernel's convolutional weights,
n_j is the number of kernels (and therefore output channels),
$\beta_k^{(j)}$ is a bias (offset), and
A_j is a nonlinear element-wise activation function, here chosen to be sigmoidal: $A_j(x) = 1/(1 + e^{-x})$, except for the last layer, where:

$$A_3(x) = \{x \text{ for } x > 0, \text{ and } e^x - 1 \text{ otherwise}\}.$$

$\boldsymbol{\alpha}^{(j)}$ represents a multi-channel set of volumes. In the case of the network's input, $\boldsymbol{\alpha}^{(1)}$, each channel could be a reconstructed modality volume such as low count $\boldsymbol{\theta}^{(100)}$ or $\boldsymbol{\theta}^{(\text{T1})}$.

For a given layer j, we will use n_j to denote the number of kernels and s_j to denote width of each kernel. The number of output channels of a layer is given by the number of kernels, and is thus also n_j.

$\boldsymbol{\kappa}^{(j)}$ corresponds to n_j different multi-channel kernels (each with $n_{j-1} \times s_j \times s_j \times s_j$ parameters) each operating on the n_{j-1}-channel input $\boldsymbol{\alpha}^{(j)}$ to produce a corresponding output channel in $\boldsymbol{\alpha}^{(j+1)}$. Each output channel can be considered to be a feature map, with the sensitivity of the corresponding feature-detecting kernel controlled by the combination of $\boldsymbol{\beta}^{(j)}$ and A_j (nonlinear thresholding). A_j is often chosen to be rectified linear units ($ReLU$) – setting negative values to zero – which performs computationally fast thresholding by simply discarding data. However, in the micro-network proposed here, such discarding is not desirable as it would result in minimal computational speed improvements at the cost of accuracy. Using sigmoids ensures that information is retained as it propagates through the network, and is discussed in more detail in Section II-C. The final layer utilises an exponential linear unit (ELU [42]) as a desirable exclusively lower-bound constraint. This acts as a weak non-negativity constraint without introducing non-linearities for positive values.

2) Micro-net: The multi-channel input $\boldsymbol{\alpha}^{(1)}$ used here includes $\boldsymbol{\theta}^{(\text{T1})}$ as well as two independent low count PET reconstructions $\boldsymbol{\theta}^{(100)}$ and $\boldsymbol{\theta}_{\text{RM}}^{(300)}$ of the same single noisy dataset. This presents the network with additional useful information – lower noise RM images as well as RM-artefact-free standard MLEM. Post-smoothed versions were not provided as the convolutional network itself is trivially capable of performing optimal (to an extent determined by the training process) spatially-invariant smoothing. T1-guided NLM was applied to the RM PET reconstruction $\boldsymbol{\theta}_{\text{RM}}^{(300)}$ using Equation (3) and also provided as an input. This allows for modulation of the PET data by the MR intensities, thereby sharing edge information. Closely approximating such an operation would normally require, for example, greater network density (increasing s_j). However this would unnecessarily greatly increase the number of optimisation parameters, thus increasing computational cost and the likelihood of overfitting on limited training data sets. Alternatively, a sufficiently deep network (increasing n_j) could also achieve the overall effect of every input pixel potentially affecting every output pixel. Adding such depth would, however, have the same caveat (as increasing s_j) of having many optimisation parameters.

In total, there are 4 different input volumes (subscripted by i in $\boldsymbol{\alpha}_{i,r}^{(1)}$ from Equation (8)): $\boldsymbol{\theta}^{(100)}$, $\boldsymbol{\theta}_{\text{RM}}^{(300)}$, $\boldsymbol{\theta}^{(\text{T1})}$, and $\text{NLM}(\boldsymbol{\theta}_{\text{RM}}^{(300)})$, each of which are independently normalised (offset to have zero mean and scaled to have unit variance).

The exception is the last case, where only the input to the NLM filter is normalised. The target is normalised to have unit variance (but no alteration of mean). This justifies the final layer's ELU activation function: large negative values should not be expected, and there should be no upper bound. This is discussed in more detail in Section II-C1. Normalisation allows the network to benefit from both PET and MR information despite their large intensity distribution differences [43].

The main network proposed here consists of three layers, with $n_1 = 32, n_2 = 32$, and $n_3 = 1$, while $s_1 = 5, s_2 = 3$, and $s_3 = 1$. The workflow to post-process with a pre-trained network would be firstly to normalise inputs, obtain a network prediction, and then multiply by a constant such that the total intensity matches the pre-normalised input. A visualisation of the network architecture is shown in Figure 1.

For comparison, different networks were trained for various choices of n_1 and n_2. The rationale is that the first layer performs detection of up to n_1 different features, and the second recombines these feature maps in different ways to produce n_2 candidate PET volumes. The final layer performs a weighted average over these volumes. The network therefore has comparatively few parameters ($\mathcal{O}(10^4)$). As the number of parameters is much lower than the size of the training data (which is $\mathcal{O}(10^7)$ even if compressed), there is no risk of overfitting, since the network is incapable of memorising the training data. This helps ensure that the network only performs feature recognition, as desired, rather than object generation. Ideally, if simulated features accurately represented real data, this would allow for training on simulated data and clinical application on real patient scans.

We propose the term micro-network or µ-net to refer to such networks which are created to be small and robust to minimal amounts of training data by design. Adding more layers to increase complexity and network depth can rapidly increase test error. Such degradation can be due to increased optimisation difficulty, and not necessarily due to overfitting [44]. Relatively shallow autoencoders perform better than deep U-nets, particularly when training data is limited [31].

Initially, two low count noise realisations of the same phantom or patient were used to create $R = 2$ sets of reconstructions (subscripted by r in $\boldsymbol{\alpha}_{i,r}^{(1)}$ from Equation (8)). The network is trained by minimising the difference between the desired target $\boldsymbol{T}$ and the current output $\boldsymbol{\alpha}^{(4)}$. This is done in batch mode (simultaneously for both sets of reconstructions). A third reconstruction set from a different phantom or patient was also used to evaluate a validation value of the loss. Training is terminated when this validation value fails to decrease for $10\,\text{k}$ epochs. The network state corresponding to minimum validation loss ($10\,\text{k}$ epochs before termination) is then restored. The training process involves the estimation of parameters
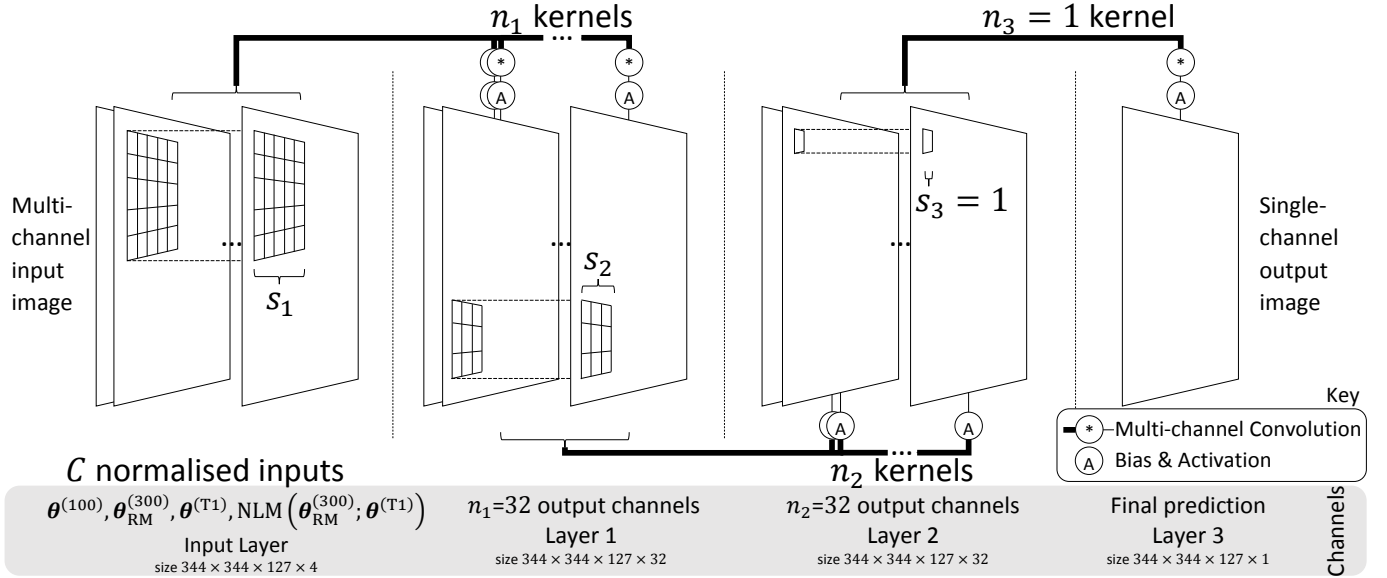
Fig. 1. Visualisation of 3-layer μ-net architecture. Note that 3D volumetric channels are depicted as 2D to ease understanding. "Multi-channel Convolution" is a many-to-one-channel operation identical to the element-wise sum of each input channel convolved with its own unique kernel. There are n_j unique kernels in each layer j. Convolutions are perfomed with stride 1 and zero padding on whole volumes without patching. For $n = \{32, 32, 1\}$ and $s = \{5, 3, 1\}$ applied to $C = 4$ input volumes, there are $43\,745$ parameters in total.

$\boldsymbol{\kappa}$ and $\boldsymbol{\beta}$ by the iterative minimisation – via gradient descent[1] – of the objective function (loss) L (Equation (9)), proportional (up to a constant) to the sample NRMSE (Equation (7)), our chosen metric of interest in this work. The loss is given by:

$$L(\boldsymbol{\kappa}, \boldsymbol{\beta}; \boldsymbol{\alpha}^{(1)}, \boldsymbol{T}) = \sqrt{\frac{1}{R} \sum_{r=1}^{R} \left\lVert \boldsymbol{T}_r - \mu_{\boldsymbol{\kappa},\boldsymbol{\beta}}(\boldsymbol{\alpha}^{(1)}_{:,r}) \right\rVert^2}, \quad (9)$$

where $\boldsymbol{\alpha}^{(1)}_{:,r}$ is the input set of 4 volumes for the rth (low count) PET noise realisation,

$\mu_{\boldsymbol{\kappa},\boldsymbol{\beta}}$ represents the application of the micro-net, such that $\mu_{\boldsymbol{\kappa},\boldsymbol{\beta}}(\boldsymbol{\alpha}^{(1)}_{:,r}) = \boldsymbol{\alpha}^{(4)}_{1,r}$,

R is the total number of low count noise realisations, and

$\boldsymbol{T}_r$ is the target PET output.

At the start of training, the weights and biases $(\boldsymbol{\kappa}, \boldsymbol{\beta})$ must be assigned starting values. *He* normal initialisation [47] was used as it was found to reduce loss by a factor of 3 compared to *LeCun* uniform initialisation [48]. The former method entails initialising $\boldsymbol{\kappa}^{(j)}$ by random normal sampling with standard deviation $\sqrt{2/n_{j-1}}$, while biases $\boldsymbol{\beta}^{(j)}$ are set to zero. This helps prevent saturation of activation functions with very large positive or negative values.

The network's biases make it possible to trivially correct for spatially-invariant bias in the input PET images. Spatially-invariant variance due to noise, however, should

be accounted for by other aspects of the network's design, so we believe a loss function susceptible to noise (in contrast to ℓ_1) is acceptable. Specifically, robustness to spatially-invariant noise is achieved by having a small architecture: the network here is certainly not dense; instead consisting of small local kernels which must be spatially invariant as they are applied to the whole input. As the kernels are optimised over the entire input, they must be able to cope with the various instances of noise found over the whole volume. The training phase should result in kernels optimised for the "average" region, which by definition has zero variance due to noise. Kernels should thus be able to compensate for spatially-invariant noise irrespective of the chosen loss function.

Since the CNN has a small receptive field (small neighbourhood width of 7 input voxels which could affect an output voxel) applied over a large volume (two orders of magnitude wider than the receptive field) it seems logical that they should not be able to compensate for spatially-variant noise. However, it is possible that based on the features detected in different spatial regions, kernels may indeed be activated by (and thus "aware of") different spatial regions, thereby handling both spatially-variant noise and bias.

While the primary objective here is to post-compensate for noise degradation, the CNN can also suppress artefacts, including the partial volume effect (PVE) and ringing.

3) U-net: For comparison, a U-net is modified to have some of the advantages of the proposed μ-net (Section II-C). These advantages include accepting normalised multi-channel inputs, as well as performing fully 3D convolutions. Optimisation details (choice of optimiser, parameter initialisation, and NRMSE loss) are kept the same as for the

micro-net.

Specifically, the U-net comprises of an "encoder" and "decoder", and a final residual layer. The encoder consists of 4 convolutional layers (with stride 2). The decoder repetitively performs trilinear upsampling (scale factor 2), concatenation with the corresponding encoder layer, and convolution (stride 1). The number of kernels per convolution layer are increased with U-net depth: $n = \{32, 64, 128, 256, 128, 64, 32, 1\}$. *ELU* activation functions are inserted for each multi-channel convolution output.

The final residual layer adds the decoder's single-channel ($n_8 = 1$) output (element-wise) to the NLM input channel (as this is the "best" input in terms of NRMSE).

C. Contributions

This work builds on and provides a novel combination of methods found in the current literature.

1) Activation functions: We use sigmoidal activation functions A_j (Equation (8)) that introduce nonlinear kernel sensitivity control. Compared to the more widely used *ReLU* (which sets negative values to zero), this is accomplished without discarding information. Note that the network's inputs and targets are normalised and thus sigmoids (which have upper bounds unlike *ReLU*) should not introduce quantification errors. Sigmoids are also easier to optimise using backpropagation due to finite curvature and a non-zero gradient, and achieve similar benefits to batch normalisation [43], [49] such as enabling higher learning rates and acting as a regulariser, thereby reducing the chance of overfitting and removing the need for dropout.

The benefit of using sigmoids (particularly for μ-nets) outweighs the increased training time compared to *ReLU*. Furthermore, sigmoids also saturate gradually (unlike *ReLU*) and thus reduce the likelihood of "deactivation" (feature maps being set to zero regardless of the input data). With the relatively small architecture proposed here, there is a low amount of redundancy built into the network, and thus such deactivation should be less encouraged.

It should however be noted that the target output (whether the ground truth or MLEM reconstruction) is strictly positive. The final layer thus requires a different activation function. However, using a *ReLU* in the final layer (while it may enforce this consistency) is not advisable. Optimisation becomes very difficult due to the sparse or "dying" *ReLU* problem [50], [51]. An exponential linear unit, *ELU* activation function is used instead. This introduces a softer minimum threshold for negative values (−1 rather than 0), while remaining linear for positive values. Compared to *ReLU* variants (including leaky, parametric, and randomised leaky *ReLU*), *ELU* has been shown to be more robust to noise and easier to optimise [42].

We found that enforcing strict non-negativity – by adding an offset of 1 or by using a plain exponential function in lieu of *ELU* – encourages undesirable saturation of the sigmoids in previous layers.

2) Fully 3D: Using 3D volumes (rather than 2D slices) means adjacent slice information is available to kernels, resulting in a superior ability to correct partial volume effects and distinguish between signal and noise.

3) Multiple realisations: For a given input noise level, training on more than one noise realisation of the same patient ($R > 1$) further increases robustness to noise at the chosen level, and reduces the need for more training data. This helps the network to detect variance and remove noise. The effect of using fewer ($R = 1$) or more ($R = 3$) training realisations is also investigated, with the expectation being that more realisations will increase network performance.

4) No patches or downsampling: Working directly on the full volumes (without subdivision into small regions and not pooling) ensures that all available data is used, without ignoring boundaries of small patches (which reduces use of adjacent voxel information to compensate for noise and PVE) and without downsampling (losing resolution unless skip connections are present). Additionally, zero padding is safe to use for convolutions without introducing edge artefacts as the whole volume is naturally zero at all boundaries. In contrast, using patches would require careful handling of edges.

5) Unity strides and no augmentation: Convolving with unity stride helps remove the need for data augmentation. Augmentations such as mirroring and rotating – which do not genuinely provide more information – also encourage rotational invariance even when the underlying system and features are not necessarily rotationally symmetric.

6) Competitive inputs: A framework which allows for alternative methods (such as NLM) to be input channels theoretically guarantees superior performance (subject to appropriate learning rates and sufficient training data). This allows the network to act as a further refinement on preprocessed input channels. It also reduces the need for density and depth. For example, NLM allows for joint edge modulation across modalities – but this would require an element-wise product between input channels – which is something a CNN can only approximate if sufficiently dense and deep. To avoid this unnecessary increase in parameters to optimise, these competitive methods may be pre-computed and supplied as inputs.

7) Optimal depth and density: The effects of varying the total number of layers, and varying the number of kernels per layer are investigated; and a network architecture is selected accordingly. It is found that a comparatively low number of kernels n_j are sufficient in each layer. This avoids redundant parameters and precludes the possibility of overfitting (memorising the training data rather than learning features). The number of optimisation parameters in a layer j is given by $(n_{j-1} \times s_j^3 + 1) \times n_j$, meaning there are a comparatively small number of parameters ($43\,745$) in total. The training data size is $\mathcal{O}(10^7)$ even when compressed; which is impossible for the network to memorise.

III. Results

The proposed and rival methods were first optimised on simulation data subjects for various count levels and targets. For testing, low count datasets from other subjects (not used during the training stage) were given to the network to make predictions for comparison to competitive methods. This process was then repeated for real data.

A. Simulations

The ground truth τ and reconstructions at different count levels for simulation subject 4 are shown in Figure 2. No other simulation subjects were used for network training.

There are 2 different input cases (3 M or 30 M counts) and 2 outputs (300 M or τ), resulting in 4 different combinations. Test metrics are all calculated against the ground truth τ (even in the case of 300 M count targets).

Four *μmu*-nets are trained separately (one for each input-output combination). Four U-nets are also trained for comparison. The loss curves for the 300 M output cases are shown in Figure 3.

Note that for each network, the input channels are as described in Section II-B2 (four channels: low count reconstructions with and without RM; T1-weighted MR, and T1-guided NLM filtering of the RM reconstruction).
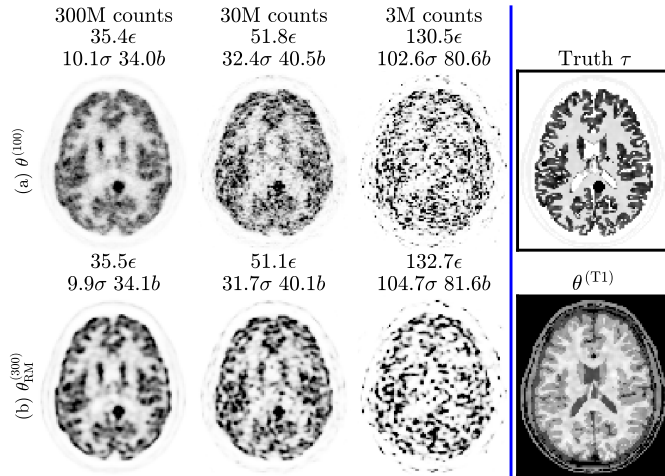

Fig. 2. Simulation training data: cropped central slices from one set of MLEM reconstructions of subject 4 at different count levels. Left panel: row a) 100 iterations of MLEM, $\boldsymbol{\theta}^{(100)}$ (showing high noise), row b) 300 iterations with RM, $\boldsymbol{\theta}^{(300)}_{\mathrm{RM}}$ (showing ringing, particularly in the grey matter at the cortical edge). NRMSE (ϵ, Equation (7)) and bias (b, Equation (5)) are calculated versus the ground truth ($\boldsymbol{\tau}$, right panel). Standard deviation (σ, Equation (6)) is calculated across 10 realisations (only one realisation is depicted).

Note that the U-net eventually achieves much lower training loss (due to its increased learning capacity) compared to the μ-net. However, the U-net easily overfits after around 50 epochs, where validation and training losses start to diverge. By comparison, when using the same data, the μ-net validation curves lie almost perfectly on top of the corresponding training curves. This demonstrates a
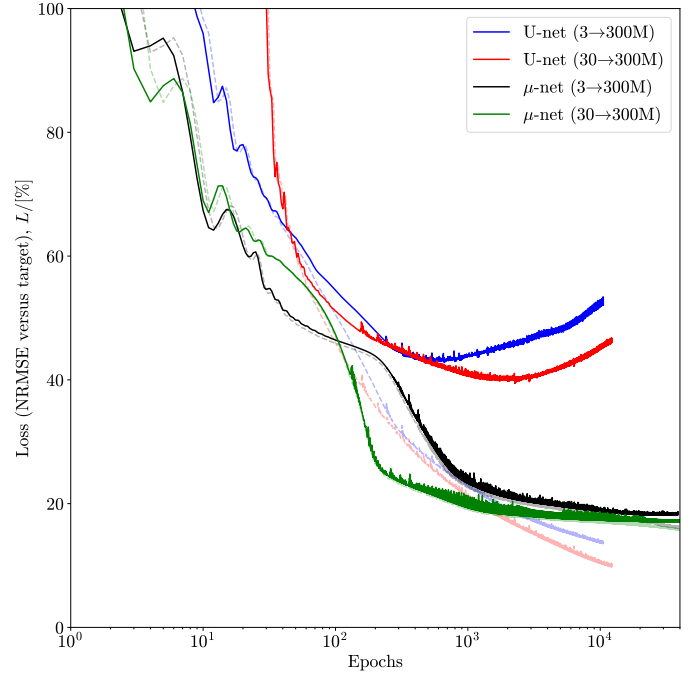

Fig. 3. Simulation loss curves for high (300 M) count targets during training on subject 4 (pale dashed lines) and validation on subject 5 (solid lines).

far superior robustness against overfitting with limited amounts of training data.

The final training outputs (predictions based on training data from Figure 2) for all four input-output cases are shown in Figure 4.
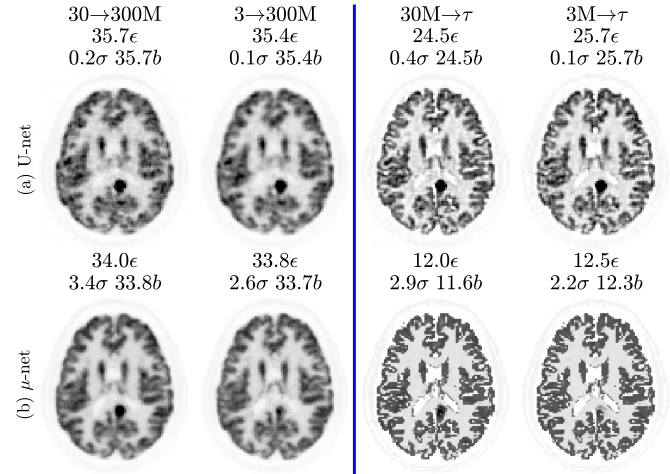

Fig. 4. Simulation **training** data predictions (compare to Figure 2). Note that the U-net has higher errors (than the μ-net) due to early termination of training (at minimum validation loss).

While both μ-nets and U-nets are capable of matching a 300 M count target, it is interesting to note that the μ-nets have half the NRMSE for a ground truth target. This is because of the early termination of training (at minimum validation loss). Figure 3 shows that for the μ-nets, this corresponds to a similarly stable and low training loss.

However, for the U-nets, training loss is still relatively high and decreasing when minimum validation loss is achieved. Training the U-nets further produces much lower training losses at the cost of higher validation losses (and thus reduced generalisability and robustness to unseen test data).

For a fair comparison to the proposed method, the smoothing kernel width (mm FWHM) and NLM parameter (Ω) are found by numerically minimising NRMSE versus the relevant target $\boldsymbol{T}$ over the training data set (subject 4).

Predictions are made based on test data (10 realisations each for 18 subjects). Results for subject 6 are shown in Figure 5. The best of the competitive methods is NLM performed on RM, except for the mapping of $30\,\mathrm{M} \rightarrow 300\,\mathrm{M}$ counts, where PS on RM produces a lower NRMSE. In all cases, the proposed method has a lower NRMSE and visually fewer artefacts.

Profiles including the lesion in Figure 5 are shown in Figure 6. Note that the μ-net simultaneously suppresses noise, partial volume, and ringing effects to match the standard count reconstruction.

Figure 7 shows bias versus standard deviation curves with increasing MLEM iterations for $30\,\mathrm{M}$ count inputs. The effects of Gaussian post-smoothing of the endpoints of MLEM reconstructions are also shown for FWHM increasing in steps of 0.1 mm. NLM filtering is also applied for $\Omega \in [10^{-5}, 10^5]$ in logarithmic steps (increments on the exponent) of 0.01. Optimal (closest to the origin, identical to minimal NRMSE) values are clearly marked. The network's output (based on low count MLEM endpoints) is comparable to the target MLEM endpoint.

The effects of different network input channels are also investigated. Various inputs are replaced with zeros and in each case the network was re-trained. Note that removing inputs altogether instead would change the network architecture. Zeroing inputs has a detrimental effect on test error in all cases. Excluding T1 information (also excluding T1-guided NLM; purely supplying MLEM and MLEM+RM) is slightly better than not including NLM and MLEM+RM (purely supplying MLEM and T1). This is interesting as it implies that (for the given noise level) RM is more important for quality improvement than T1 information. Ideally the networks should be re-trained several times in order to produce confidence intervals to verify this.

An ℓ_1-norm may be used instead of ℓ_2 (Equation (9)) "to encourage less blurring" [52]. While both would be susceptible to noise, ℓ_1 may be less so. We have thus also included results for an otherwise identical μ-net trained with an ℓ_1 loss function for comparison. As expected, this results in a slightly higher NRMSE (minimising ℓ_2 is identical to minimising NRMSE, unlike ℓ_1).

Furthermore, it is interesting to note that re-training the network with more ($R = 3$) realisations evidently has negligible improvement, while using fewer ($R = 1$) has very little detriment.

Note that a network trained to match the ground truth $\boldsymbol{\tau}$ (also shown) has built-in information about reconstruction bias which neither PS nor NLM alone could compensate for.

A similar graph for $3\,\mathrm{M}$ counts is shown in Figure 8. This makes it clearer that omitting RM information harms network performance more than omitting T1 information does. There is also a slight improvement as training realisations R increase from 1 to 2, and a negligible improvement from 2 to 3.

Note that several different μ-networks were trained with various numbers of layers J and choices of kernel numbers n_j per layer in order to find an optimal combination. n_j were always set to be the same for all hidden ($j \in [1, J)$) layers, and increased from 1 to 256 in powers of 2. Note that the final n_J can only be 1 due to requiring only one output channel. An investigation of different architectures showed that $n_j = 32$ kernels were sufficient in all cases. Figure 9 shows NRMSE for the case of $3\,\mathrm{M}$ to $300\,\mathrm{M}$ counts mapping. Error increases slightly for larger n. As discussed in Section II-B2, it is possible that this is due to increased optimisation difficulty rather than overfitting.

B. Real Data

Reconstructions for training (patient 1) – similar to the simulations in Figure 2 – are shown in Figure 10. Standard deviation σ can be calculated across multiple realisations by resampling the raw data as mentioned in Section II-A2.

Apart from being based on real PET data acquisitions, a big difference between simulations and real data is the nature of the MR information. The real T1 images are lower resolution, contain artefacts, have different noise properties, and are not perfectly registered.

Test data and the corresponding μ-net prediction are shown in Figure 11. Note that since the ground truth is unknown, metrics are calculated with reference to the full count reconstruction $\boldsymbol{\theta}_{\text{full}}^{(100)}$.

IV. Conclusion

The simulations results clearly show that application of a *upmu*-net always produces lower NRMSE than post-smoothing or NLM filtering (see Figure 7 and Figure 8). The micro-network predictions in Figure 5(h) also show much less noise – a reduction in standard deviation σ by a factor of up to 3 compared to rivals (c)-(f) – and lower bias. The exception is the case of mapping $30\,\mathrm{M} \rightarrow 300\,\mathrm{M}$, where a slightly higher σ than NLM is compensated for by the lower bias to still produce a lower overall NRMSE (visible in Figure 7). This reduction is achieved without sacrificing image resolution.

Future work will need to consider the impact of mismatched noise levels (testing on different noise levels than used for
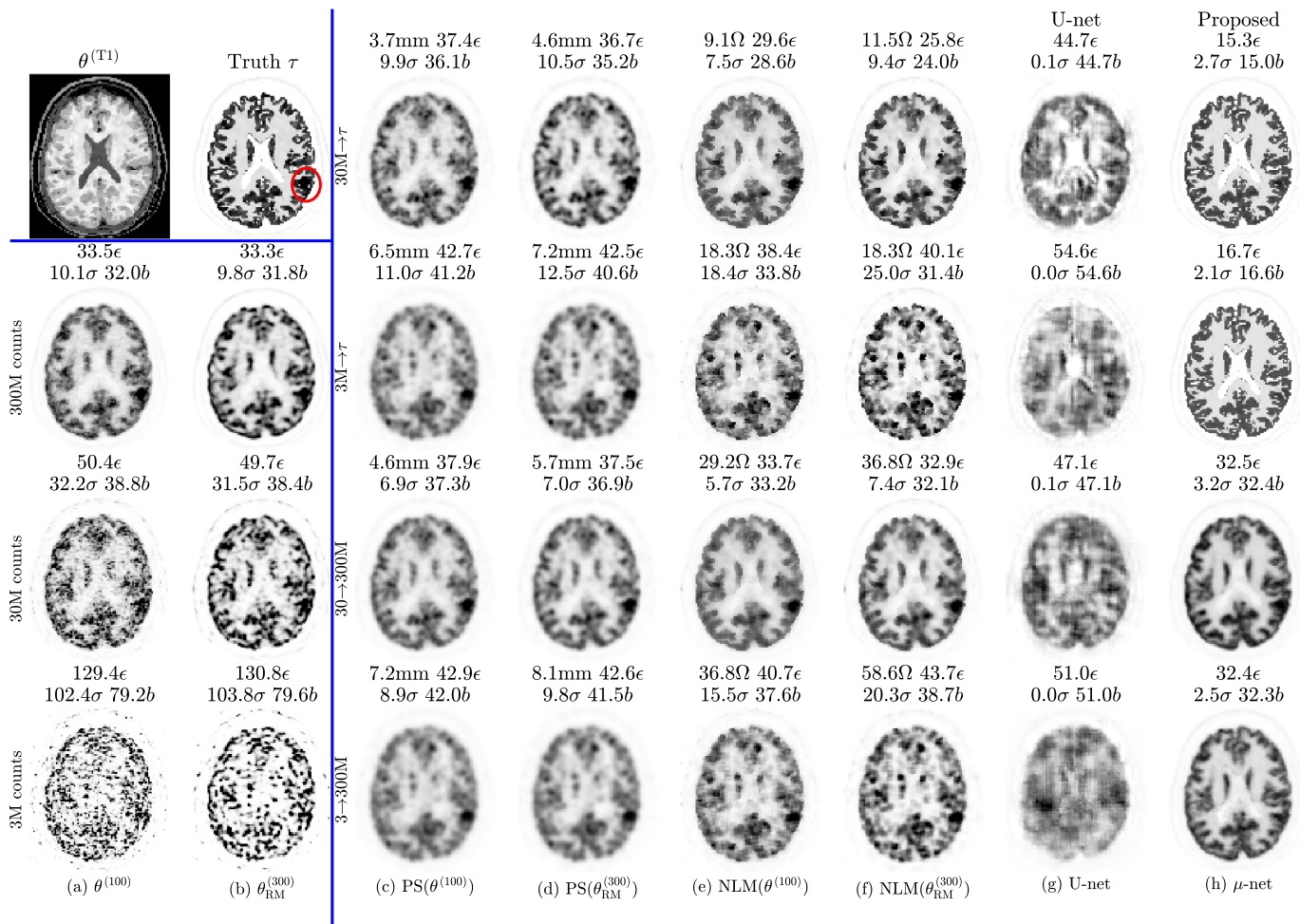
Fig. 5. Simulation **test** data: cropped central slices from one set of MLEM reconstructions of subject 6 at different count levels without (a) and with (b) resolution modelling. For comparison (c)-(f) and proposed (h) methods, optimisation is performed to minimise NRMSE between the training input and target. This is given by the row titles, which are labelled according to "input → optimisation target" (see Figure 2 for corresponding training data images). NRMSE ϵ and bias b metrics are calculated versus the known ground truth τ. Standard deviation σ is across 10 realisations. Optimal values are given in panel titles for smoothing FWHM (mm) and NLM parameter (Ω).
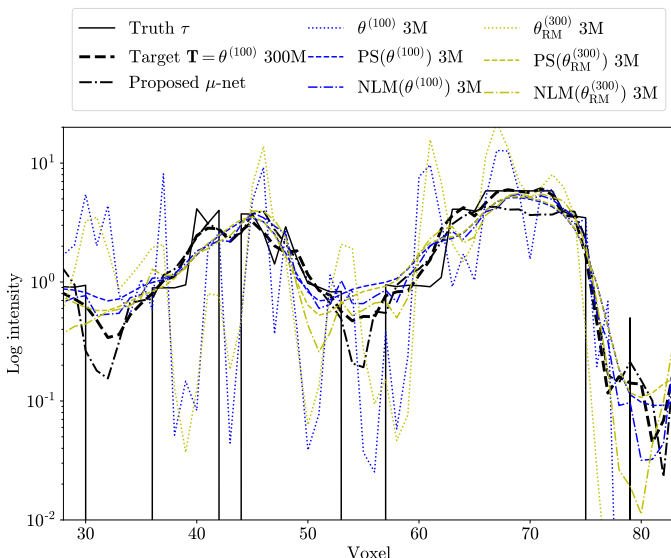

Fig. 6. Test data profiles (horizontal line through the lesion circled in Figure 5 τ) for 3 M→300 M counts mapping.

training), as well as using one architecture to compensate for noise and artefacts at different noise levels and at different iterations of MLEM (rather then re-training a network for each case). Increasing the number of training data sets will also produce a more robust network with even better resolution recovery and artefact suppression properties. It would also be interesting to investigate why simply providing more low count reconstructions of the same patient during the training phase (increasing R) does not seem to significantly increase network robustness to noise. Generative adversarial networks (GANs), which can be used to augment data sets [53], have been recently applied to low dose PET [52], [54]. It would be particularly interesting in future work to combine the methods proposed here in a GAN framework. The network could also easily be extended to include joint modality (synergistic) post-processing such as PET-guided undersampled MR reconstruction, or even modality generation such as PET prediction based on MR.
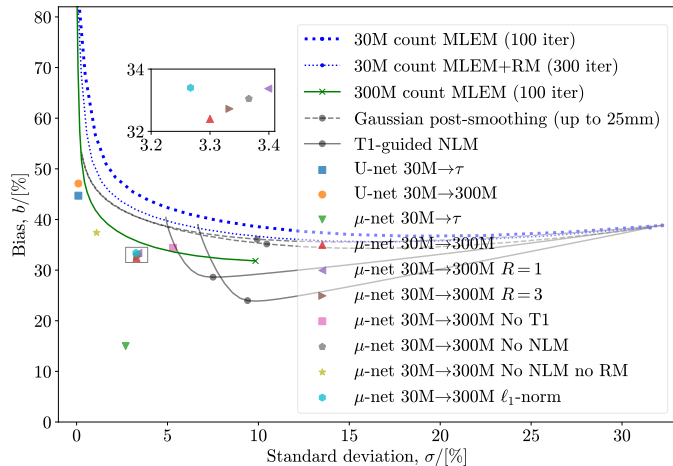
Fig. 7. Test bias versus standard deviation. Distance from the origin corresponds to NRMSE (note that the axes have different scales). Standard (300 M) and low (30 M) count curves show the trade-off with increasing MLEM iterations (endpoints marked with crosses). Gaussian PS of increasing FWHM and NLM filtering with increasing Ω are also depicted with optimal values circled. The proposed network's prediction based on low count inputs has comparable bias and much lower standard deviation compared to the target standard count reconstruction. Unless specified otherwise, $R = 2$ realisations of one patient were used to train each network.
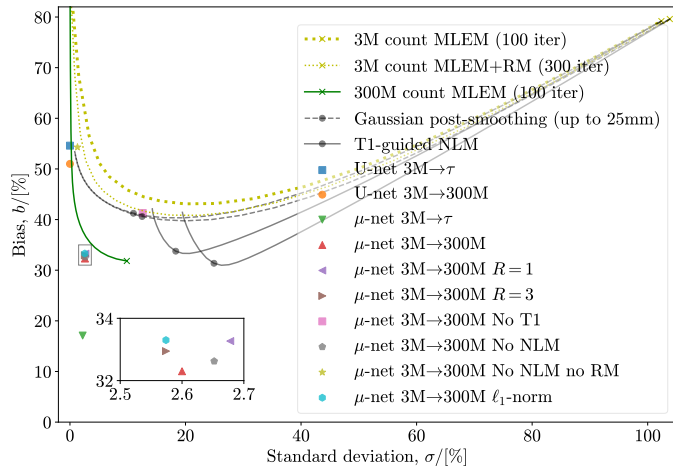

Fig. 9. Effect of varying number of layers J and number of kernels per layer n_j on **test** NRMSE (for 3 M→300 M counts mapping, calculated versus truth $\boldsymbol{\tau}$). For each choice of layers J, the number of kernels n_j is set to 1 for all hidden layers. The number of kernels per layer n_j is then increased from 1 up to 256 in powers of 2 to produce the curves above. Due to memory constraints, it was only possible to reach up to $n_j = 16$ and 8 kernels per layer for $J = 5$ and 6 layers, respsectively.

Fig. 8. Test bias versus standard deviation for very low (3 M) counts, similar to Figure 7.
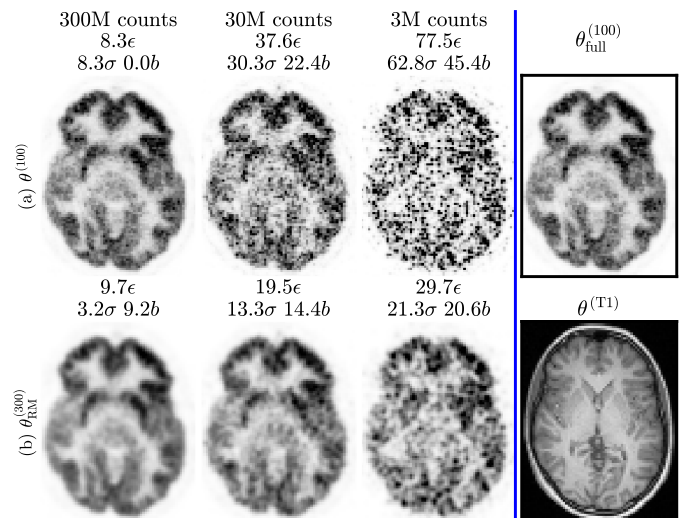
Fig. 10. Real patient training data: cropped central slices from MLEM reconstructions of patient 1 following the same layout as Figure 2. NRMSE ϵ and bias b are calculated against the full count reconstruction $\boldsymbol{\theta}_{\text{full}}^{(100)}$ (black rectangle), including for the bootstrap sampled 300 M (standard) count target $\boldsymbol{T}$. Standard deviation σ can be estimated since 10 realisations were generated for each count level.

V. References

[1] C. Cloquet and M. Defrise, "MLEM and OSEM deviate from the cramer-rao bound at low counts," *IEEE Trans Nucl. Sci.*, vol. 60, no. 1, pp. 134–143, 2013, doi: 10.1109/TNS.2012.2217988.

[2] T. Chang, G. Chang, J. W. Clark, R. H. Diab, E. Rohren, and O. R. Mawlawi, "Reliability of predicting image signal-to-noise ratio using noise equivalent count rate in PET imaging," *Med. Phys*, vol. 39, no. 10, pp. 5891–5900, Sep. 2012, doi: 10.1118/1.4750053.

[3] S. Tong, a M. Alessio, and P. E. Kinahan, "Noise and signal properties in PSF-based fully 3D PET image reconstruction: an experimental evaluation." *Phys Med. Biol.*, vol. 55, no. 5, pp. 1453–1473, 2010, doi: 10.1088/0031-9155/55/5/013.

[4] F. L. Andersen, T. L. Klausen, A. Loft, T. Beyer, and S. Holm, "Clinical evaluation of PET image reconstruction using a spatial resolution model," *Eur. J. Radiol.*, vol. 82, no. 5, pp. 862–869, 2013, doi: 10.1016/j.ejrad.2012.11.015.

[5] A. M. Alessio, A. Rahmim, and C. G. Orton, "Resolution modeling enhances PET imaging," *Med. Phys*, vol. 40, no. 12, p. 120601, 2013, doi: 10.1118/1.4821088.

[6] A. Rahmim, J. Qi, and V. Sossi, "Resolution modeling in PET imaging: Theory, practice, benefits, and pitfalls," *Med. Phys*, vol. 40, no. 6, p. 064301, 2013, doi: 10.1118/1.4800806.

[7] S.-L. Hu, Z.-Y. Yang, Z.-R. Zhou, X.-J. Yu, B. Ping, and Y.-J. Zhang, "Role of SUVmax obtained by 18F-FDG

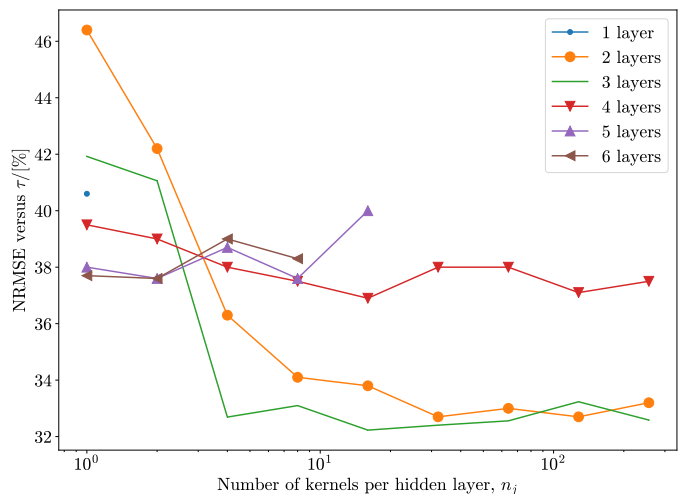3M counts
88.9ε
71.9σ 52.2b

30M counts
36.8ε
29.4σ 22.1b

300M counts
10.1ε
10.1σ 0.0b

$\theta^{(\mathrm{T1})}$

$\theta^{(100)}$

33.8ε
24.6σ 23.2b

17.5ε
10.7σ 13.9b

10.5ε
4.0σ 9.7b

$\theta^{(100)}_{\mathrm{full}}$

$\theta^{(300)}_{\mathrm{RM}}$

$\theta^{(100)}$ 30M counts $\theta^{(300)}_{\mathrm{RM}}$
3mm 19.5ε   4.5mm 17.0ε
13.6σ 14.0b   5.7σ 16.0b

$\theta^{(100)}$ 3M counts $\theta^{(300)}_{\mathrm{RM}}$
7.2mm 23.8ε   8.6mm 25.0ε
10.1σ 21.6b   6.7σ 24.1b

PS

73.9Ω 18.9ε   0.03Ω 17.5ε
6.3σ 17.8b   10.7σ 13.9b

187Ω 26.6ε   93.3Ω 24.8ε
14.5σ 22.3b   11.1σ 22.2b

NLM

U-net
18.0ε
7.8σ 16.3b

μ-net
16.5ε
7.0σ 15.0b

U-net
38.0ε
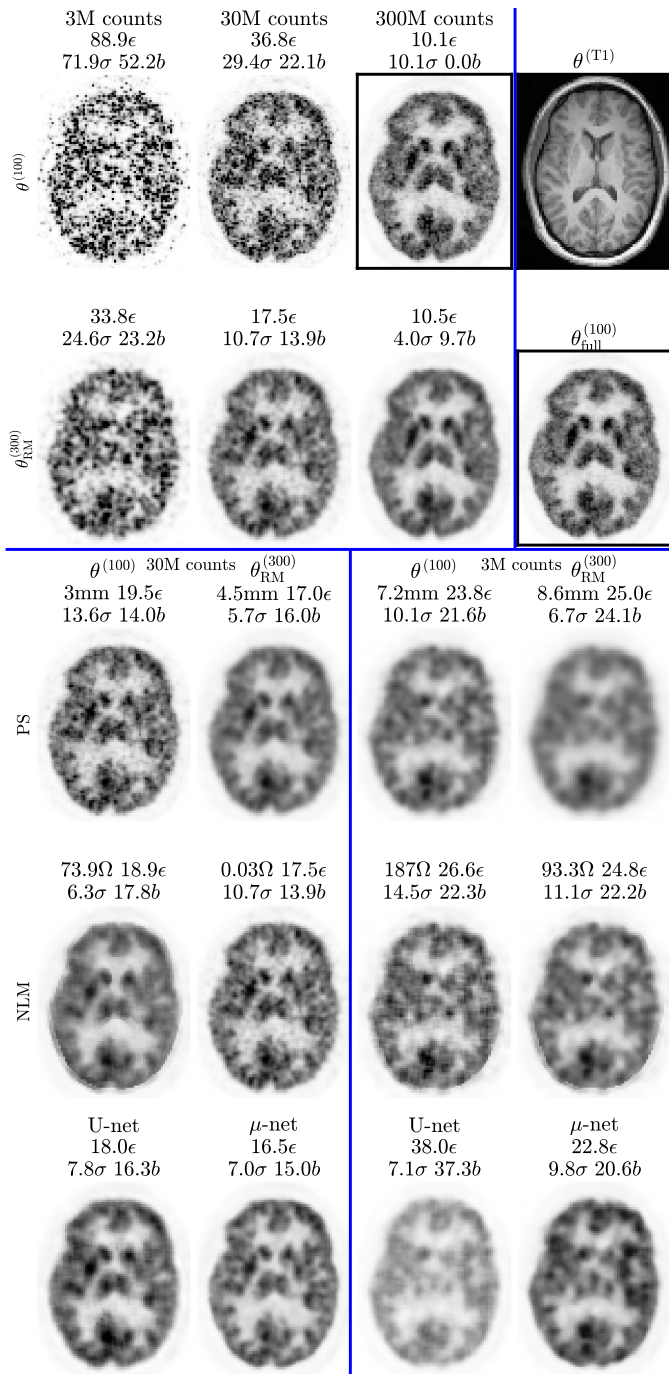7.1σ 37.3b

μ-net
22.8ε
9.8σ 20.6b

Fig. 11. Real patient test results: cropped central slices from MLEM reconstructions of patient 2. There are two images in black boxes: the 300 M reconstruction depicted is a target T for comparison, while the full count reconstruction $\theta^{(100)}_{\mathrm{full}}$ (without bootstrap sampling) was used as a reference to calculate bias and standard deviation (including for the target T).

PET/CT in patients with a solitary pancreatic lesion," *Nucl. Med. Commun.*, vol. 34, no. 6, pp. 533–539, 2013, doi: 10.1097/MNM.0b013e328360668a.

[8] O. L. Munk, L. P. Tolbod, S. B. Hansen, and T. V. Bogsrud, "Point-spread function reconstructed PET images of sub-centimeter lesions are not quantitative," *EJNMMI Phys*, vol. 4, no. 1, p. 5, 2017, doi: 10.1186/s40658-016-0169-9.

[9] S. Stute and C. Comtat, "Practical considerations for image-based PSF and blobs reconstruction in PET," *Phys Med. Bio.*, vol. 58, no. 11, p. 3849, 2013.

[10] A. Mikhno, E. D. Angelini, B. Bai, and A. F. Laine, "Locally weighted total variation denoising for ringing artifact suppression in pet reconstruction using PSF modeling," in *Proc. Int. Symp. Biomed. Imaging*, 2013, pp. 1252–1255, doi: 10.1109/ISBI.2013.6556758.

[11] M. S. Tahaei, A. J. Reader, and D. L. Collins, "MR-guided PET image denoising," in *2016 IEEE Nucl. Sci. Symp. Med. Imaging Conf. Proc. (NSS/MIC)*, 2016, pp. 1–3, doi: 10.1109/NSSMIC.2016.8069564.

[12] J. Bland *et al.*, "MR-Guided Kernel EM Reconstruction for Reduced Dose PET Imaging," *IEEE Trans Rad. Plasma Med. Sci.*, vol. 2, no. 3, pp. 235–243, May 2018, doi: 10.1109/TRPMS.2017.2771490.

[13] J. Tang, B. Yang, Y. Wang, and L. Ying, "Sparsity-constrained PET image reconstruction with learned dictionaries," *Phys Med. Biol.*, vol. 61, no. 17, p. 6347, 2016.

[14] Y. Cong, S. Zhang, and Y. Lian, "K-SVD dictionary learning and image reconstruction based on variance of image patches," in *8th ISCID*, 2015, vol. 2, pp. 254–257, doi: 10.1109/ISCID.2015.148.

[15] Z. Guo, X. Li, H. Huang, N. Guo, and Q. Li, "Deep Learning-Based Image Segmentation on Multimodal Medical Imaging," *IEEE Trans Rad. Plasma Med. Sci.*, vol. 3, no. 2, pp. 162–169, Mar. 2019, doi: 10.1109/TRPMS.2018.2890359.

[16] G. Litjens *et al.*, "A Survey on Deep Learning in Medical Image Analysis," *Med. Image Anal.*, vol. 42, pp. 60–88, Feb. 2017, doi: 10.1016/j.media.2017.07.005.

[17] G. Pereira, P. H. Abreu, I. Domingues, P. Martins, H. Duarte, and J. Santos, "Using deep learning techniques to CT, PET and PET/CT in medical imaging : a systematic review," *Artif. Intell. Rev.*, 2018.

[18] C. O. da Costa-Luis and A. J. Reader, "Deep Learning for Suppression of Resolution-Recovery Artefacts in MLEM PET Image Reconstruction," in *2017 IEEE Nucl. Sci. Symp. Med. Imaging Conf. Proc. (NSS/MIC)*, 2017, pp. 1–3, doi: 10.1109/NSSMIC.2017.8532624.

[19] C. O. da Costa-Luis and A. J. Reader, "Convolutional micro-networks for MR-guided low-count PET image processing," in *2018 IEEE Nucl. Sci. Symp. Med. Imaging Conf. Proc. (NSS/MIC)*, 2018, pp. 1–4, doi: 10.1109/NSSMIC.2018.8824373.

[20] K. Gong, J. Guan, C.-C. Liu, and J. Qi, "PET Image Denoising Using a Deep Neural Network Through Fine Tuning," *IEEE Trans Rad. Plasma Med. Sci.*, vol. 3, no. 2, pp. 153–161, Mar. 2019, doi: 10.1109/TRPMS.2018.2877644.

[21] J. Schlemper, J. Caballero, J. V. Hajnal, A. Price, and D. Rueckert, "A Deep Cascade of Convolutional Neural Networks for MR Image Reconstruction," vol. 10265, M. Niethammer et al., Eds. Springer International Publishing, 2017, pp. 647–658.

[22] S. Kaplan and Y.-M. Zhu, "Full-Dose PET Image Estimation from Low-Dose PET Image Using Deep Learning: a Pilot

Study," *J. Digit. Imaging*, vol. 3, Nov. 2018, doi: 10.1007/s10278-018-0150-3.

[23] J. Jiao and S. Ourselin, "Fast PET reconstruction using Multi-scale Fully Convolutional Neural Networks," *ArXiv e-prints*, Apr. 2017 [Online]. Available: https://arxiv.org/abs/1704.07244

[24] H. Chen *et al.*, "Low-dose CT via convolutional neural network," *Biomed. Opt. Express*, vol. 8, no. 2, pp. 679–694, Feb. 2017, doi: 10.1364/BOE.8.000679.

[25] L. Xiang *et al.*, "Deep auto-context convolutional neural networks for standard-dose PET image estimation from low-dose PET/MRI," *Neurocomputing*, vol. 267, pp. 406–416, Dec. 2017, doi: 10.1016/j.neucom.2017.06.048.

[26] K. Gong *et al.*, "Iterative PET Image Reconstruction Using Convolutional Neural Network Representation," *IEEE Trans Med. Imaging*, vol. 38, no. 3, pp. 1–1, Oct. 2018, doi: 10.1109/TMI.2018.2869871.

[27] B. Yang, L. Ying, and J. Tang, "Artificial neural network enhanced bayesian PET image reconstruction," *IEEE Trans Med. Imaging*, vol. 0062, no. c, pp. 1–1, 2018, doi: 10.1109/TMI.2018.2803681.

[28] Y. Wang *et al.*, "Predicting standard-dose PET image from low-dose PET and multimodal MR images using mapping-based sparse representation," *Phys Med. Bio.*, vol. 61, no. 2, pp. 791–812, 2016, doi: 10.1088/0031-9155/61/2/791.

[29] L. An *et al.*, "Multi-Level Canonical Correlation Analysis for Standard-Dose PET Image Estimation," *IEEE Trans Image Proc.*, vol. 25, no. 7, pp. 3303–3315, Jul. 2016, doi: 10.1109/TIP.2016.2567072.

[30] J. Kang, Y. Gao, F. Shi, D. S. Lalush, W. Lin, and D. Shen, "Prediction of standard-dose brain PET image by using MRI and low-dose brain [^{18}F]FDG PET images," *Med. Phys*, vol. 42, no. 9, pp. 5301–5309, 2015, doi: 10.1118/1.4928400.

[31] H. Lim, I. Y. Chun, Y. K. Dewaraja, and J. A. Fessler, "Improved low-count quantitative PET reconstruction with a variational neural network," pp. 1–11, Jun. 2019 [Online]. Available: http://arxiv.org/abs/1906.02327

[32] J. Xu, E. Gong, J. Pauly, and G. Zaharchuk, "200x Low-dose PET Reconstruction using Deep Learning," Dec. 2017 [Online]. Available: http://arxiv.org/abs/1712.04119

[33] C. Cocosco, V. Kollokian, R.-S. Kwan, and A. Evans, "BrainWeb: Online Interface to a 3D MRI Simulated Brain Database," *NeuroImage*, vol. 5, no. 4, pp. 2/4, S425, 1997.

[34] C. O. da Costa-Luis, "BrainWeb-based multimodal models of 20 normal brains." Jul-2019 [Online]. Available: https://doi.org/10.5281/zenodo.3269888

[35] P. J. Markiewicz *et al.*, "NiftyPET: a High-throughput Software Platform for High Quantitative Accuracy and Precision PET Imaging and Analysis," *Neuroinformatics*, vol. 16, no. 1, pp. 95–115, Jan. 2018, doi: 10.1007/s12021-017-9352-y.

[36] D. L. Snyder and M. I. Miller, "The use of sieves to stabilize images produced with the em algorithm for emission tomography," *IEEE Trans Nucl. Sci.*, vol. 32, no. 5, pp. 3864–3872, Oct. 1985, doi: 10.1109/TNS.1985.4334521.

[37] A. Buades, B. Coll, and J.-M. Morel, "A Non-Local Algorithm for Image Denoising," in *2005 IEEE Comput. Soc. Conf. Comput. Vis. Pattern Recognit. (CVPR)*, 2005, vol. 2, pp. 60–65, doi: 10.1109/CVPR.2005.38.

[38] G. Wang and J. Qi, "PET Image Reconstruction Using Kernel Method," *IEEE Trans Med. Imaging*, vol. 34, no. 1, pp. 61–71, Jan. 2015, doi: 10.1109/TMI.2014.2343916.

[39] P. J. Markiewicz *et al.*, "Rapid processing of PET list-mode data for efficient uncertainty estimation and data analysis," *Phys Med. Biol.*, vol. 61, no. 13, pp. N322–N336, Jul. 2016, doi: 10.1088/0031-9155/61/13/N322.

[40] V. Y. Panin, M. Chen, and C. Michel, "Simultaneous update iterative algorithm for variance reduction on random coincidences in PET," in *2007 IEEE Nucl. Sci. Symp. Conf. Rec.*, 2007, vol. 4, pp. 2807–2811, doi: 10.1109/NSSMIC.2007.4436722.

[41] E. Garyfallidis *et al.*, "Dipy, a library for the analysis of diffusion MRI data," *Frontiers in Neuroinformatics*, vol. 8, no. February, pp. 1–17, Feb. 2014, doi: 10.3389/fninf.2014.00008.

[42] D.-A. Clevert, T. Unterthiner, and S. Hochreiter, "Fast and Accurate Deep Network Learning by Exponential Linear Units (ELUs)," *4th Int. Conf. Learn. Rep. (ICLR) 2016 - Conf. Track Proc.*, pp. 1–14, Nov. 2015 [Online]. Available: http://arxiv.org/abs/1511.07289

[43] S. Ioffe and C. Szegedy, "Batch Normalization: Accelerating Deep Network Training by Reducing Internal Covariate Shift," Feb. 2015 [Online]. Available: http://arxiv.org/abs/1502.03167

[44] K. He, X. Zhang, S. Ren, and J. Sun, "Deep Residual Learning for Image Recognition," Dec. 2015 [Online]. Available: http://arxiv.org/abs/1512.03385

[45] M. Abadi *et al.*, "TensorFlow: Large-scale machine learning on heterogeneous systems." 2015 [Online]. Available: https://www.tensorflow.org/

[46] D. P. Kingma and J. Ba, "Adam: A Method for Stochastic Optimization," Dec. 2014 [Online]. Available: http://arxiv.org/abs/1412.6980

[47] K. He, X. Zhang, S. Ren, and J. Sun, "Delving Deep into Rectifiers: Surpassing Human-Level Performance on ImageNet Classification," *Proc. IEEE Int. Conf. Comput. Vis. (ICCV)*, vol. 2015 Inter, pp. 1026–1034, Feb. 2015, doi: 10.1109/ICCV.2015.123. [Online]. Available: http://arxiv.org/abs/1502.01852

[48] Y. A. LeCun, L. Bottou, G. B. Orr, and K.-R. Müller, "Efficient backprop," in *Neural networks: Tricks of the trade: Second edition*, G. Montavon et al., Eds. Berlin, Heidelberg: Springer Berlin Heidelberg, 2012, pp. 9–48.

[49] Z. Liao and G. Carneiro, "On the importance of normalisation layers in deep learning with piecewise linear activation units," in *2016 IEEE Winter Conf. Appl. Comput. Vis. (WACV)*, 2016, pp. 1–8, doi: 10.1109/WACV.2016.7477624.

[50] B. Xu, N. Wang, T. Chen, and M. Li, "Empirical Evaluation of Rectified Activations in Convolutional Network," May 2015 [Online]. Available: http://arxiv.org/abs/1505.00853

[51] P. Henderson, R. Islam, P. Bachman, J. Pineau, D. Precup, and D. Meger, "Deep Reinforcement Learning that Matters," in *AAAI conf. artif. intell.*, 2018.

[52] Y. Wang *et al.*, "3D conditional generative adversarial networks for high-quality PET image estimation at low dose," *NeuroImage*, vol. 174, no. March, pp. 550–562, Jul. 2018, doi: 10.1016/j.neuroimage.2018.03.045.

[53] M. Mirza and S. Osindero, "Conditional Generative Adversarial Nets," pp. 1–7, 2014 [Online]. Available: http://arxiv.org/abs/1411.1784

[54] Y. Wang *et al.*, "3D Auto-Context-Based Locality Adaptive Multi-Modality GANs for PET Synthesis," *IEEE Trans Med. Imaging*, vol. 38, no. 6, pp. 1328–1339, Jun. 2019, doi: 10.1109/TMI.2018.2884053.